

Realising equal strength welding to parent metal in precipitation-hardened Al–Mg–Si alloy via low heat input friction stir welding

X. H. Zeng, P. Xue, D. Wang, D. R. Ni, B. L. Xiao & Z. Y. Ma

To cite this article: X. H. Zeng, P. Xue, D. Wang, D. R. Ni, B. L. Xiao & Z. Y. Ma (2018) Realising equal strength welding to parent metal in precipitation-hardened Al–Mg–Si alloy via low heat input friction stir welding, *Science and Technology of Welding and Joining*, 23:6, 478-486, DOI: [10.1080/13621718.2017.1415249](https://doi.org/10.1080/13621718.2017.1415249)

To link to this article: <https://doi.org/10.1080/13621718.2017.1415249>



Published online: 20 Dec 2017.



Submit your article to this journal [↗](#)



Article views: 101



View related articles [↗](#)



View Crossmark data [↗](#)



Citing articles: 1 View citing articles [↗](#)



Realising equal strength welding to parent metal in precipitation-hardened Al–Mg–Si alloy via low heat input friction stir welding

X. H. Zeng^{a,b}, P. Xue^a, D. Wang^a, D. R. Ni^a, B. L. Xiao^a and Z. Y. Ma^a

^aShenyang National Laboratory for Materials Science, Institute of Metal Research, Chinese Academy of Sciences, Shenyang, People's Republic of China; ^bUniversity of Chinese Academy of Sciences, Beijing, People's Republic of China

ABSTRACT

Two millimetres thick Al–Mg–Si (6061Al–T6) alloy plates were friction stir welded at various welding conditions. Under a low rotation rate of 400 rev min⁻¹ with rapid water cooling, the softening zone in the joint disappeared and a nanostructure with an average grain size of 80 nm was obtained in the stir zone (SZ). Therefore, a weld with equal strength to the parent metal (PM) was successfully achieved with the fracture occurring in the PM. Further, the average microhardness and ultimate tensile strength (UTS) of the SZs increased with the decreasing rotation rate and increasing cooling speed. The average microhardness and UTS of the SZ with nanostructure reached up to 134 HV and 505 MPa, respectively; though the initial strengthened precipitates disappeared. This work provides an effective strategy of achieving high property joints and enhancing the mechanical properties of precipitation-hardened Al alloys.

ARTICLE HISTORY

Received 17 October 2017
Accepted 6 December 2017

KEYWORDS

Precipitation-hardened Al alloy; friction stir welding; nanostructured grains; strength

Introduction

Al–Mg–Si alloy is a typical precipitation-hardened alloy with Mg–Si typed precipitates. This alloy is usually used in a T6 temper state (artificially peak aged), with the metastable β'' being the main strengthening precipitates [1]. For conventional fusion welding, the high heat input not only causes the severe grain coarsening, but also leads to the dissolution of the β'' precipitates in the weld nugget [2]. Furthermore, an overaged structure with coarsened β phase is observed in the heat-affected zone (HAZ) due to the low aging temperature of Al–Mg–Si alloy (~ 448 K) [3].





Obviously, dissolution and coarsening of the precipitates result in a distinct softening zone in the HAZ, producing dramatic loss of the hardness and strength of the joint compared to those of the parent metal (PM) [4]. Traditionally, it is believed that it is impossible to obtain an equal strength joint to the PM in T6-treated Al–Mg–Si alloys.

Friction stir welding (FSW), as a solid-state joining technique with many advantages over the conventional fusion welding methods, has been widely used in various industries involving Al alloys [5–8]. However, conventional FSW still creates an obvious softening region in the HAZ in the T6-treated Al–Mg–Si alloys, resulting in joint efficiencies of only 60–75% [9,10]. Water cooling [11,12] was proven to be an effective method of reducing the heat input during FSW and inhibiting the softening of the HAZ where significantly reduced

peak temperature and duration at high temperature were achieved.

It is encouraging that FSW joints with near-equal strength to the PM can be obtained in cold-rolled pure copper and 5083Al–H19 by forced water cooling [11,13]. However, previous study also indicated that the softening zone still existed in the FSW joints of precipitation-hardened Al alloys with the peak aged state [14]. Therefore, the heat input should be reduced further in order to obtain equal strength joint to the PM. Usually, using smaller shoulder is an effective strategy of decreasing heat input during FSW [15,16]. Thus, using smaller shoulder with additional cooling is a possible method of inhibiting the softening of the HAZ.

It is well known that grain refinement can enhance the mechanical properties for most metals and alloys, and severe plastic deformation (SPD) is an effective method of achieving ultrafine-grained (UFG) materials [17]. Further, low deformation temperature is beneficial to producing finer grains [18,19], and nanostructured grains (< 100 nm) could be obtained by SPD under ultra-high strain and strain rate, such as high-pressure torsion (HPT) [18,19] and surface mechanical attrition treatment (SMAT) [20,21]. Therefore, as an SPD process with ultra-high strain and strain rate [22,23], FSW under extremely low heat input is a potential method of enhancing the mechanical properties of the stir zone (SZ) via obvious structure refinement [24].

CONTACT P. Xue  pxue@imr.ac.cn  Shenyang National Laboratory for Materials Science, Institute of Metal Research, Chinese Academy of Sciences, 72 Wenhua Road, Shenyang 110016, People's Republic of China; Z. Y. Ma  zyma@imr.ac.cn  Shenyang National Laboratory for Materials Science, Institute of Metal Research, Chinese Academy of Sciences, 72 Wenhua Road, Shenyang 110016, People's Republic of China

In this study, FSW was conducted on 2 mm thick 6061Al-T6 plates using a small shoulder with additional cooling. It is expected that this process could inhibit the softening in the HAZ completely and refine the grains in the SZ greatly. The aim of this study is to achieve high property FSW joint with equal strength to the PM and enhancing the mechanical properties of the SZ.

Experimental procedure

Commercial 6061Al-T6 plates 2 mm in thickness were used in this study. First, stir-in-plate FSW was employed on the plates in order to optimise the welding parameter; then, butt FSW was conducted with the optimum parameter. During FSW with water cooling, the plates were first fixed in water and additional rapid cooling with flowing water was used. At the same time, normal FSW process with air cooling was performed in order to make a comparison.

In order to reduce the heat input, a tool with a concave shoulder 8 mm in diameter and a conical threaded pin 3 mm in root diameter and 1.8 mm in length was used. FSW was conducted at a constant traverse speed of 100 mm min^{-1} with different tool rotation rates of 400 and $1000 \text{ rev min}^{-1}$, defined 400-A and 1000-A for normal FSW samples, and 400-W and 1000-W for samples with water cooling, respectively.

The cross-sections of FSW 6061Al-T6 joints perpendicular to the welding direction was subjected to macrostructural observations by optical microscopy (OM). After grinding and polishing, the samples were etched by Keller's etching reagent which includes 2 ml HF, 3 ml HCl, 5 ml HNO_3 , and 190 ml H_2O . The grain size and precipitates in the SZ were investigated using transmission electron microscopy (TEM) combined with scanning transmission electron microscopy (STEM) and energy dispersive spectroscopy. TEM foil specimens were prepared by twin jet electro-polishing using a solution of 30 ml HNO_3 and 70 ml CH_3OH at a temperature of 248 K and a voltage of 10 V.

Vickers microhardness measurement was conducted on the cross-section perpendicular to the welding direction along the mid-thickness of the joints under a load of 50 g for a holding time of 15 s. The mini-specimens of the SZs were machined parallel to the

welding direction with a gauge length of 2.5 mm. Meanwhile, large tensile specimens of FSW joints were machined perpendicular to the welding direction with a gauge length of 40 mm. All the tensile tests were conducted at room temperature and were operated at an initial strain rate of $1 \times 10^{-3} \text{ s}^{-1}$.

Results

Macrostructural and microstructural characterisation

Figure 1 shows the cross-sectional macrostructures of the FSW samples with various parameters. It is clear that no defects were detected under the investigated welding parameters. All the FSW samples exhibited basin-shaped SZs with wide top regions, and the macrostructure of the SZ was significantly influenced by the FSW parameters. It is clear that the SZ size was determined by both rotation rate and cooling method. With increasing the tool rotation rate, the SZ became larger no matter under air cooling or water cooling. At the same time, the SZ under air cooling was larger than that under water cooling. Further, according to the corrosion contrasts of SZs, the macrostructure of the SZ of 400-W sample (hereafter defined as 400-W SZ) was the most uniform.

Figure 2 shows the bright-field TEM images and statistical distributions of the grain size of the SZs in all FSW samples, and the grain sizes were measured by the linear intercept method. It is clear that equiaxed ultra-fine grains were observed in the SZs of 400-A, 1000-A, and 1000-W samples (Figure 2(a,e, and g)), and the average grain sizes were determined to be 0.49 ± 0.16 , 1.54 ± 0.31 , and $0.84 \pm 0.18 \mu\text{m}$ (Figure 2(b, f, and h)), respectively. It is clear that both rotation rate and cooling speed determined the grain size in the SZ. The grain size of the SZ became smaller as the tool rotation rate decreased. Furthermore, the grain size decreased clearly under water cooling compared to that under air cooling at the same rotation rate of $1000 \text{ rev min}^{-1}$.

Different from other FSW samples, many elongated grains were observed in the 400-W SZ besides the equiaxed grains, as shown in Figure 2(c). More importantly, the microstructure exhibited nanostructured characteristic, and the average grain size measured by linear intercept method (length of brachyaxis

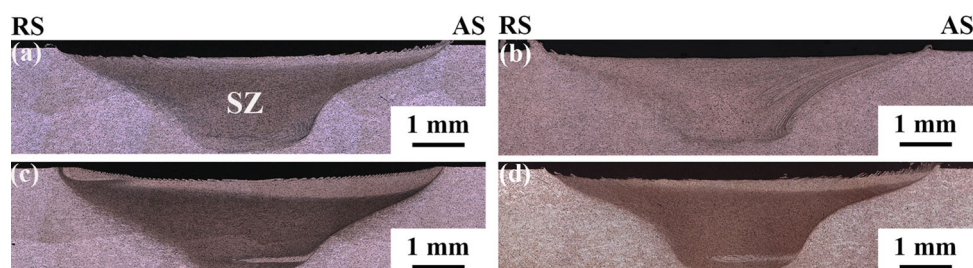


Figure 1. Macrostructural characterisation of FSWed 6061Al-T6: (a) 400-A, (b) 400-W, (c) 1000-A, and (d) 1000-W.

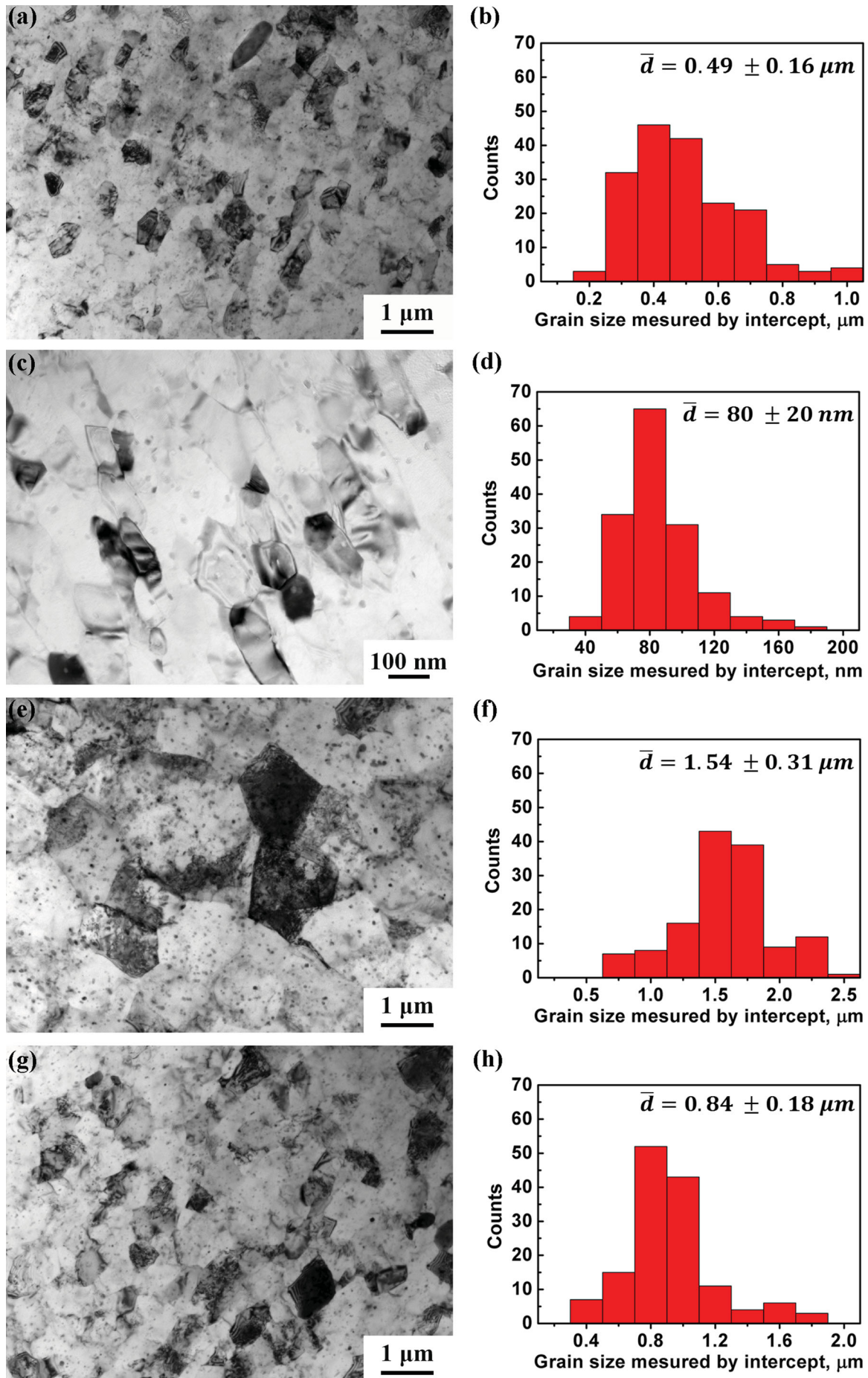


Figure 2. The grain structures and statistical distributions of the grain size measured by linear intercept method in the SZs: (a) and (b) 400-A, (c) and (d) 400-W, (e) and (f) 1000-A, and (g) and (h) 1000-W.

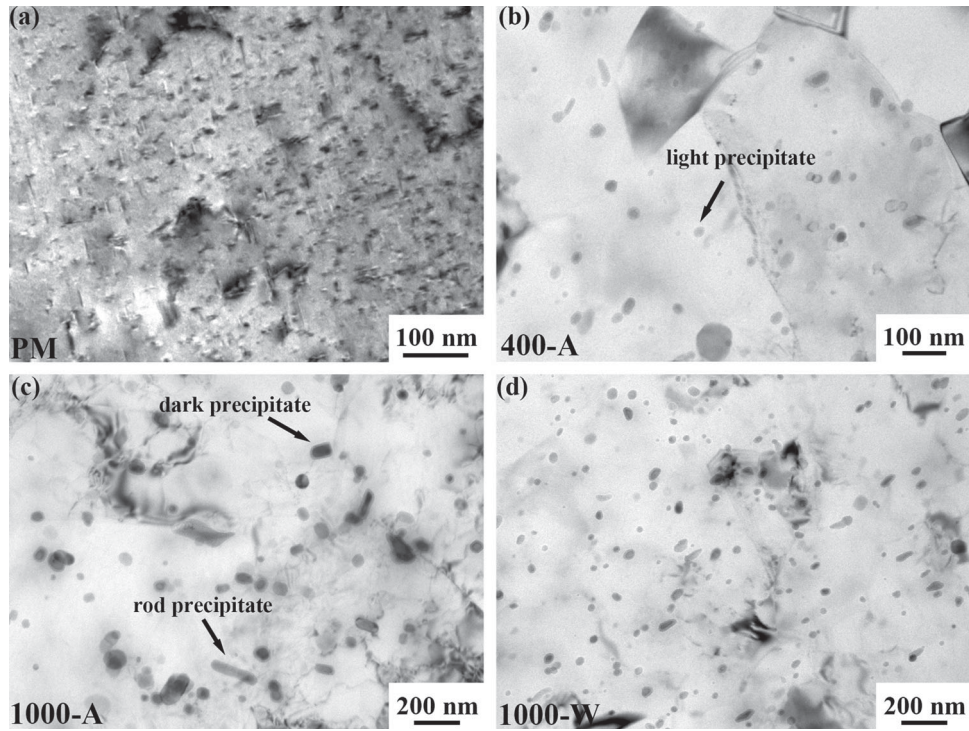


Figure 3. TEM micrographs of precipitated phase in the PM and SZs: (a) PM, (b) 400-A, (c) 1000-A, and (d) 1000-W.

for elongated grains) was calculated to be 80 ± 20 nm (Figure 2(d)).

Figure 3 shows the magnified bright-field TEM images of the precipitates in the PM and the SZs of 400-A, 1000-A, and 1000-W samples, respectively. The PM exhibited a typical precipitation-strengthened structure of Al–Mg–Si alloys with lots of needle-like β''

precipitates (Figure 3(a)). However, large numbers of spherical particles were observed in the SZs of 400-A, 1000-A, and 1000-W samples, with the average size being about 20, 60, and 30 nm, respectively. These spherical precipitates can be divided into two categories: light and dark precipitates, as shown in Figure 3(b–d). Moreover, some rodlike precipitates with a

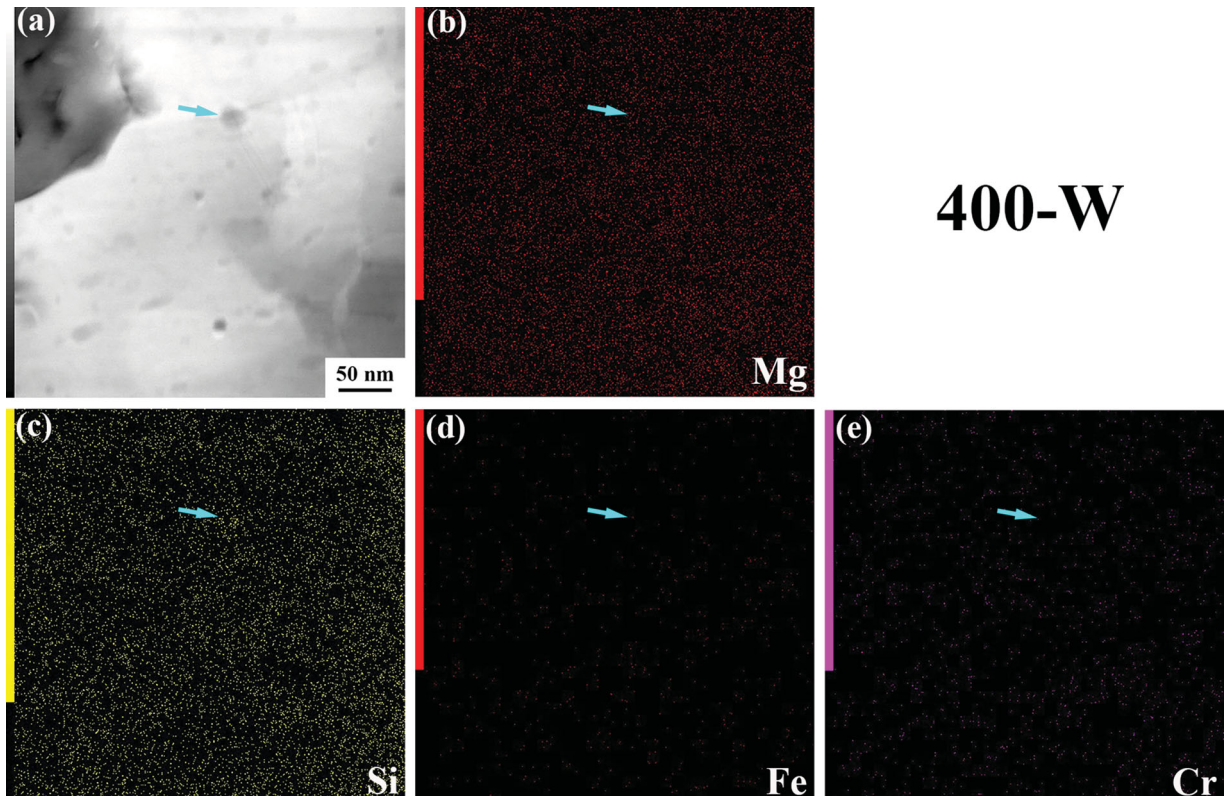


Figure 4. (a) STEM bright-field image and corresponding EDS mappings with (b) Mg, (c) Si, (d) Fe, and (e) Cr for 400-W SZ.

length of about 200 nm could be observed in the 1000-A SZ.

Differently, few light spherical precipitates were found in the 400-W SZ, and the average size of the spherical particles was only about 10 nm, as shown in Figure 2(c). These light spherical particles were also observed in HPT Al–Mg–Si alloy by Sauvage et al. [19] and the particles could be either β or β' , according to analyses of the diffraction patterns and Mg–Si ratio [19]. Therefore, the number and size of the precipitates in the SZs were closely related to the rotation rate and cooling conditions during the FSW process.

Figures 4 and 5 show the STEM bright-field images and EDS mappings of precipitates in the 400-W and 1000-A SZs, respectively. The light spherical precipitates in the 400-W SZ were identified to the Mg-rich and Si-rich particles, as shown in Figure 4. Similar to those in the 400-W SZ, the light spherical precipitates rich in Mg and Si were also observed in the 1000-A SZ. Moreover, the rodlike precipitates in this sample were also rich in Mg and Si, as can be clearly seen in Figure 5. Besides these precipitates, the EDS mapping also reveals that there were dark particles rich in Si, Fe, and Cr as marked by a green arrow in Figure 5(a–e). These dark particles were also observed in HPT Al–Mg–Si alloy by Mohamed et al. [18].

Mechanical properties

Figure 6 shows the microhardness profiles of the FSW samples under various parameters and cooling

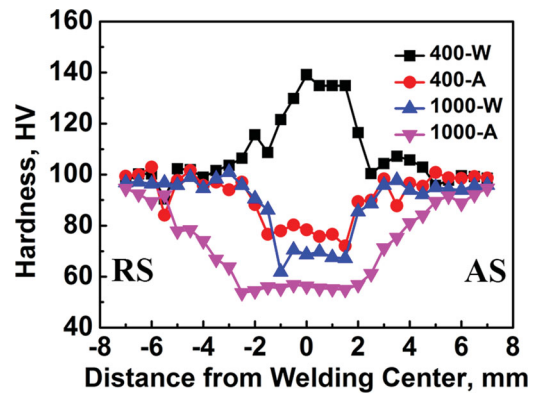


Figure 6. The microhardness profiles of the FSW samples under various parameters and cooling conditions.

conditions. The hardness profiles of 400-A and 1000-W samples both exhibited a typical ‘W’ shape with two low hardness zones (LHZs) near the SZ, which was similar to those of most FSW Al–Mg–Si alloy joints [9,25]. The average hardness values in the 400-A and 1000-W SZs were about 75 and 70 HV, respectively, which were lower than those of the PM (~ 100 HV). Obvious softening occurred in 1000-A sample and the average hardness value in the 1000-A SZ was only about 55 HV. By comparison, no obvious softening was observed in 400-W sample from the hardness profile. The average hardness value of the SZ was as high as 134 HV, which was even higher than that of the PM with the T6 state.

Figure 7(a) shows the engineering stress–strain curves of the PM and SZs of various FSW joints. The

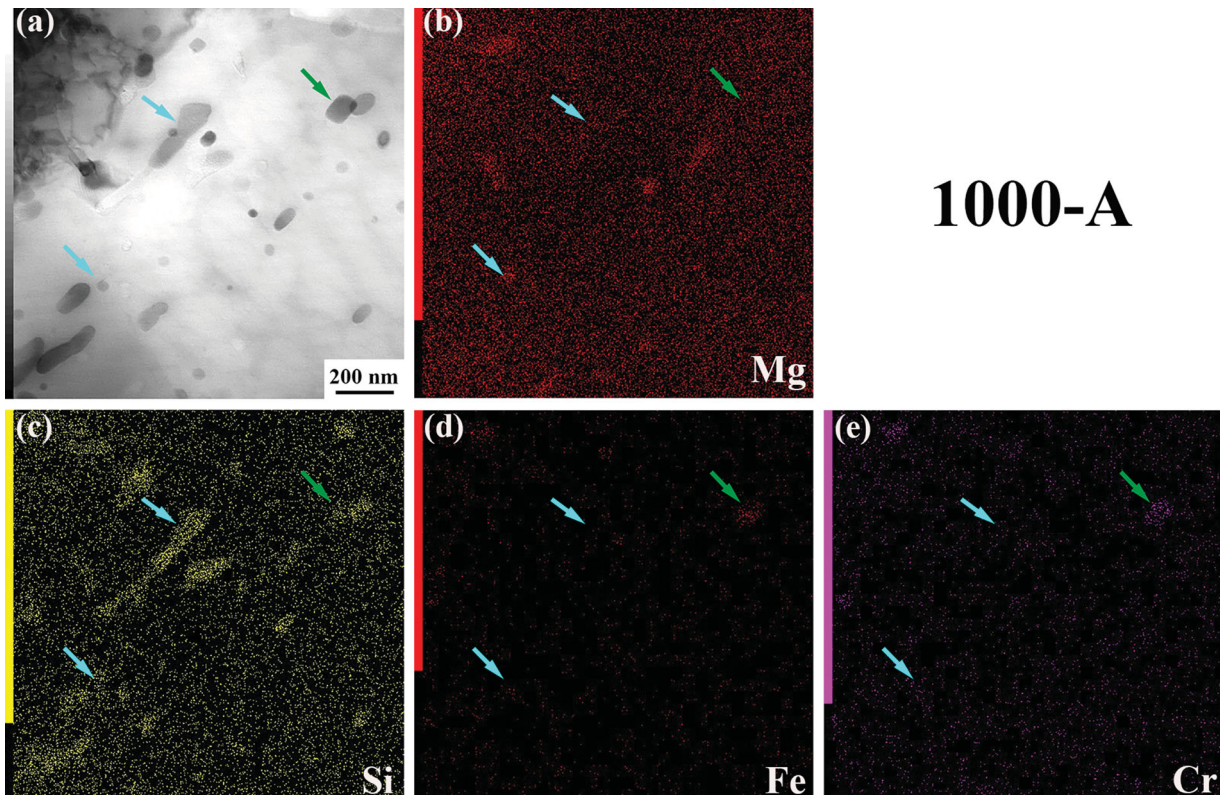


Figure 5. (a) STEM bright-field image and corresponding EDS mappings with (b) Mg, (c) Si, (d) Fe, and (e) Cr for 1000-A SZ.

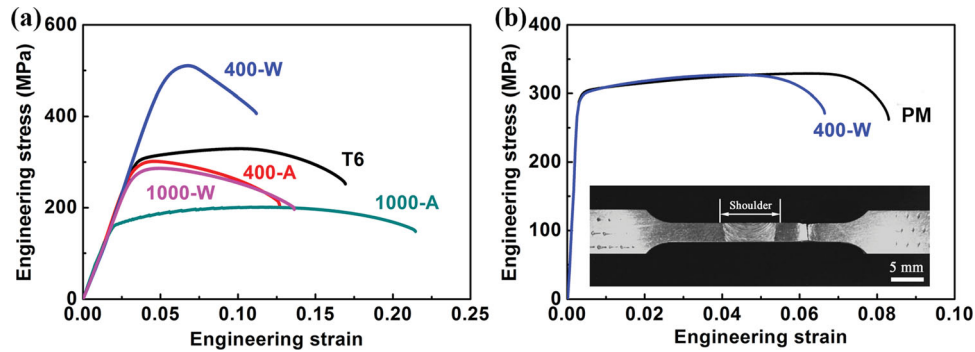


Figure 7. (a) The engineering stress–strain curves of the PM and SZs of various FSW joints; and (b) the engineering stress–strain curves of the 6061Al-T6 PM and 400-W FSW joints.

yield strength (YS) and ultimate tensile strength (UTS) of the 1000-A SZ were only 158 and 200 MPa, respectively. By applying the rapid water cooling, the YS and UTS of the 1000-W SZ increased to 270 and 287 MPa, respectively. However, the elongation was only about 2%. The YS of the 400-A SZ increased to an equivalent value of the PM (290 MPa), and exhibited similar tensile curves to that of the 1000-W SZ. For the 400-W SZ, it is clear that significantly enhanced tensile strength was achieved compared to the PM, and the YS and UTS increased to 495 and 505 MPa, respectively.

Figure 7(b) shows the engineering stress–strain curves of the PM and 400-W joint. It is clear that the engineering stress–strain curve of the 400-W joint was almost the same as that of the PM, except the slightly reduced elongation. The 400-W joint fractured at the PM side, resulting in the same strength to that of the PM. Therefore, equal strength welding to the PM was successfully achieved in 6061Al-T6 alloy.

Discussion

Grain size and precipitates in SZ

It has been demonstrated in the FSW of Al alloys that the formation of fine grains in the SZ is attributed to dynamic recrystallization (DRX) due to the intense plastic deformation and thermal exposure [26]. So far, three types of DRX mechanisms, i.e. continuous dynamic recrystallization, discontinuous dynamic recrystallization (DDR), and geometric dynamic recrystallization (GDRX), have been proposed as the main grain evolution mechanisms during the FSW of Al alloys [26–28].

Owing to the decreased heat input, the grain size of the SZ became smaller with decreasing the tool rotation rate, which can be clearly seen in Figure 2. Furthermore, Yazdipour et al. [28] reported that finer grains could be obtained during FSW with high cooling rate. The cooling rate of water cooling condition was higher than that of air cooling condition and the heat input could be further reduced by the enhanced heat transfer from the tool and plate into the surrounding water in this study [11]. Thus, the grain size of the SZ under water cooling was obviously finer than that under air cooling at the same rotation rate.

Like other SPD materials, UFG is one of the main characteristics of FSW alloys [24,29]. Excitingly, nanostructured and elongated grains were obtained in the 400-W SZ (Figure 2(b)). Owing to the low rotation rate and rapid water cooling in the 400-W sample, there are no sufficient energy and time to recrystallise and grow for the deformed grains. Thus, the average size of final grains in the 400-W SZ was about 80 nm and part of grains remained the original deformed morphology.

It is well known that the grain sizes for various plastic deformation methods are generally decided by the strain and strain rate in the grain refinement process [17]. Table 1 shows the comparisons of strain, strain rate, the achieved minimum grain size, and grain shape in Al–Mg–Si alloys and pure Al prepared by various processing techniques. It is clear that the nanostructured grains could be obtained by HPT, FSW, and SMAT methods due to the ultra-high strain and strain rate [18–23]. Moreover, it is worth noting that the nanostructured grains in the top surface of SMAT samples are elongated grains or lamellar structures [20], which were also observed in the 400-W SZ in this study.

Table 1. The strain, strain rate, the minimum grain size, grain shape, and tensile properties of FSW Al–Mg–Si alloy and other SPD Al–Mg–Si alloys or pure Al.

Fabrication method	Strain	Strain rate (s^{-1})	Minimum grain size (nm)	Grain shape	UTS (MPa)	References
ARB	4	< 10	300	equiaxed	362	[30]
ECAP	8	–	200	equiaxed	405	[31,32]
HPT	100	< 25	100	equiaxed	460	[18]
FSW/P	35	75	80	equiaxed/elongated	505	[22,23]
SMAT (pure Al)	20–45	$\sim 10^3$	30	elongated/lamellar	–	[20]

Based on the EDS mapping and previous reports [19,33], the light spherical precipitates rich in Mg and Si in the 400-W and 1000-A SZs should be Mg_2Si particles. Owing to the increased heat input, the light spherical particles coarsened with increasing the rotation rate, especially under air cooling, as shown in Figures 2(c) and 3(b–d). Usually, these spherical particles are the typical morphology characteristics of particles observed in SPD Al–Mg–Si alloys [18,33,34]. High strain is applied to the material during the SPD process, which changes the orientation of the precipitates. Further, the loss of low-energy interfaces between precipitates and the Al matrix causes the particles to grow into an equiaxed morphology [34]. Thus, the spherical morphology of the particles is very different from the typical rod-shaped morphology observed in the conventional Al–Mg–Si alloy after peak-aging or over-aging. Moreover, due to high heat input and long duration at high temperature, the rodlike precipitates rich in Mg and Si, similar to those observed in overaged Al–Mg–Si alloys [1], were observed in the 1000-A SZ (Figure 3(c)).

Relationship between microstructures and properties

It is commonly accepted that the hardness contribution of each microstructural features can be added as follows:

$$HV = HV^{Al} + \Delta HV^{GB} + \sum_i \Delta HV_i^{sol} + \Delta HV^{precip} + \Delta HV^{dislo}, \quad (1)$$

where HV^{Al} is the hardness of pure Al, ΔHV^{GB} is the grain boundary hardening, ΔHV_i^{sol} is the solute hardening, ΔHV^{precip} is the precipitate hardening, and ΔHV^{dislo} is the strain hardening resulting from dislocations. Such a rough estimate, considering a simple additive contribution of each feature, has already been successfully applied to understand the hardness evolution of the SPD materials [18,19].

For 400-W sample, few precipitates and dislocations were found in the SZ (Figure 2(c)); therefore, precipitate hardening and dislocation hardening effects can be ruled out.

The relationship between the grain boundary and the yield stress or hardness of materials has been suggested by Hall and Petch a long time ago, which can be extended to Al alloys processed by SPD [18,19]. Sato et al. [35] reported that the hardness of an FSW 1050Al could be written as:

$$HV = 18 + 19d^{-\frac{1}{2}}, \quad (2)$$

where d is the grain size. In this equation, the hardness of pure Al is 18 HV and only the grain size contribution would be taken into account. Thus, for 400-W sample, $\Delta HV^{GB} = 19d^{-\frac{1}{2}} = 68HV$.

The influence of solute hardening on the yield stress has been investigated by Myhr et al. [36] and it can be written as:

$$\Delta \sigma_i = k_i C_i^{\frac{2}{3}}, \quad (3)$$

where $\Delta \sigma_i$ is the absolute increase in yield stress due to the solute i , C_i is the concentration and k_i is a scaling factor for the i solute. They have proposed the following value for Mg and Si solutes: $k_{Mg} = 29 \text{ MPa (wt-\%)}^{-2/3}$ and $k_{Si} = 66.3 \text{ MPa (wt-\%)}^{-2/3}$ [36]. Then, the absolute increase in yield stress due to Mg and Si solutes in 6061Al is determined to be $\Delta \sigma_i = 84 \text{ MPa}$. For SPD Al–Mg–Si alloy, a ratio σ_y/HV of about 2 has been identified by Sauvage et al. [19]. Thus, for the 400-W sample, the solute hardening by Mg and Si solutes is determined to be $\Delta HV^{sol} = 42HV$.

Based on the above analyses, the estimated hardness in the 400-W SZ is 128 HV, which is well accord with the experimental value (134 HV). Following this approach, it is obvious that nanostructured grain is the prime factor for the high hardness in the 400-W SZ.

Similarly, the grain size is the main influencing factor for the tensile properties of SPD Al alloys [18,30]. The elongation of 400-A, 400-W, and 1000-W SZs were only about 2–3%, as shown in Figure 7(a), which was similar to other UFG Al alloys [30,31]. Owing to the coarsened spherical particles, the UTS of 400-A and 1000-W SZs were only 287 and 200 MPa, respectively. The tensile properties are summarised in Table 1 with comparison with other SPD Al–Mg–Si alloys. Clearly, due to finer grain size achieved by FSW, the tensile strength of the 400-W SZ was even higher than that of the Al–Mg–Si alloy prepared by some SPD methods, such as ARB, ECAP, and HPT [18,30,31].

For the precipitation-hardened aluminium alloys, the FSW joints often fractured at the LHZ due to significant dissolution/coarsening of the precipitates during the welding thermal cycle [15, 25]. Thus, the lowest hardness value is the key factor for the tensile properties of the FSW joints. The lowest hardness values in various welded joints of 6061Al-T6 are shown in Figure 8. It is clear that most of the lowest hardness values

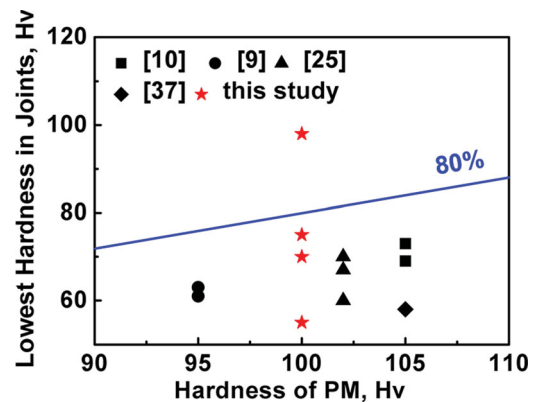


Figure 8. The lowest hardness values in various weld 6061Al-T6 joints.

in welded 6061Al-T6 joints were lower than 80% PM hardness. Only the lowest hardness of FSW 6061Al-T6 joint under 400 rev min⁻¹ with water cooling in this study reached the PM hardness. That is to say, the mechanical properties of the HAZ were similar to those of the PM in the FSW joint of 400-W sample. This is reason for the 400-W joint to fracture at the PM side. Thus, the engineering stress-strain curve of the 400-W joint was almost the same as that of the PM, except the slightly reduced elongation due to the strain concentration in a shorter region resulting from higher strength in the SZ. This study distinctly provides an effective method of realising equal strength welding to the PM for the high strength metals and alloys.

Conclusions

Friction stir welding (FSW) with small shoulder under water cooling condition was used to achieve high property FSW joints and enhance the mechanical properties of Al-Mg-Si alloy. The conclusions drawn from the results can be summarised as follows:

- (1) With decreasing rotation rate and increasing cooling speed, the grain size in the SZ decreased for 6061Al-T6 alloy. Under a rotation rate of 400 rev min⁻¹ and rapid water cooling condition, the nanostructure with an average grain size of 80 nm was obtained in the SZ.
- (2) The average hardness and UTS of the SZs increased with the decreasing rotation rate and increasing cooling speed, and reached up to 134 HV and 505 MPa respectively, for 400 rev min⁻¹ and rapid water cooling conditions.
- (3) Under a low rotation rate of 400 rev min⁻¹ with rapid water cooling, the softening zone in the HAZ disappeared and a weld with equal strength to the PM was achieved with the fracture occurring in the PM. This study provides an effective method of realising equal strength welding to the PM.

Disclosure statement

No potential conflict of interest was reported by the authors.

Funding

This work was supported by the National Natural Science Foundation of China under grant numbers (51301178 and 51331008).

References

- [1] Edwards GA, Stiller K, Dunlop GL, et al. The precipitation sequence in Al-Mg-Si alloys. *Acta Mater.* 1998;46:3893–3904.
- [2] Peng D, Shen J, Tang Q, et al. Effects of aging treatment and heat input on the microstructures and mechanical properties of TIG-welded 6061-T6 alloy joints. *Int J Min Met Mater.* 2013;20:259–265.
- [3] Dutta I, Allen SM. A calorimetric study of precipitation in commercial aluminium alloy 6061. *Mater Sci Lett.* 1991;10:323–326.
- [4] Abúndez A, Pereyra I, Campillo B, et al. Improvement of ultimate tensile strength by artificial ageing and retrogression treatment of aluminium alloy 6061. *Mater Sci Eng A.* 2016;668:201–207.
- [5] Xu RZ, Ni DR, Yang Q, et al. Influence of Zn coating on friction stir spot welded magnesium-aluminium joint. *Sci Technol Weld Joining.* 2017;6:512–519.
- [6] Nandan R, Debroy T, Bhadeshia HKDH. Recent advances in friction-stir welding – process, weldment structure and properties. *Prog Mater Sci.* 2008;53:980–1023.
- [7] Huang YX, Han B, Lv SX, et al. Interface behaviours and mechanical properties of filling friction stir weld joining AA 2219. *Sci Technol Weld Joining.* 2012;17:225–230.
- [8] Zhao K, Liu ZY, Xiao BL, et al. Friction stir welding of carbon nanotubes reinforced Al-Cu-Mg alloy composite plates. *J Mater Sci Technol.* 2017;33:1004–1008.
- [9] Lee WB, Yeon YM, Jung SB. Mechanical properties related to microstructural variation of 6061 Al alloy joints by friction stir welding. *Mater Trans.* 2004;45:1700–1705.
- [10] He J, Ling Z, Li H. Effect of tool rotational speed on residual stress, microstructure, and tensile properties of friction stir welded 6061-T6 aluminum alloy thick plate. *Int J Adv Manuf Technol.* 2016;84:1953–1961.
- [11] Xue P, Xiao BL, Zhang Q, et al. Achieving friction stir welded pure copper joints with nearly equal strength to the parent metal via additional rapid cooling. *Scr Mater.* 2011;64:1051–1054.
- [12] Zhang H, Liu H. Mathematical model and optimization for underwater friction stir welding of a heat-treatable aluminum alloy. *Mater Des.* 2013;45:206–211.
- [13] Wang BB, Chen FE, Liu F, et al. Enhanced mechanical properties of friction stir welded 5083Al-H19 joints with additional water cooling. *J Mater Sci Technol.* 2017;33:1009–1014.
- [14] Zhang Z, Xiao BL, Ma ZY. Influence of water cooling on microstructure and mechanical properties of friction stir welded 2014Al-T6 joints. *Mater Sci Eng A.* 2014;614:6–15.
- [15] Zhang XX, Xiao BL, Ma ZY. A transient thermal model for friction stir weld. Part II: effects of weld conditions. *Metall Mater Trans A.* 2011;42:3218–3228.
- [16] Rai R, De A, Bhadeshia HKDH, et al. Review: friction stir welding tools. *Sci Technol Weld Joining.* 2011;16:325–342.
- [17] Adachi N, Todaka Y, Irie K, et al. Phase transformation kinetics of ω -phase in pure Ti formed by high-pressure torsion. *J Mater Sci.* 2016;51:2608–2615.
- [18] Mohamed IF, Lee S, Edalati K, et al. Aging behavior of Al 6061 alloy processed by high-pressure torsion and subsequent aging. *Metall Mater Trans A.* 2015;46:2664–2673.
- [19] Sauvage X, Bobruk EV, Murashkin MY, et al. Optimization of electrical conductivity and strength combination by structure design at the nanoscale in Al-Mg-Si alloys. *Acta Mater.* 2015;98:355–366.
- [20] Chang HW, Kelly PM, Shi YN, et al. Thermal stability of nanocrystallized surface produced by surface mechanical attrition treatment in aluminum alloys. *Surf Coat Technol.* 2012;206:3970–3980.
- [21] Yang H, Wu X, Yang Z, et al. Enhanced boronizing kinetics of alloy steel assisted by surface mechanical attrition treatment. *J Alloys Compd.* 2014;590:388–395.

- [22] Xu S, Deng XM. A study of texture patterns in friction stir welds. *Acta Mater* **2008**;56:1326–1341.
- [23] Liu XC, Wu CS, Padhy GK. Characterization of plastic deformation and material flow in ultrasonic vibration enhanced friction stir welding. *Scr Mater*. **2015**;102:95–98.
- [24] Xue P, Huang Z, Wang B, et al. Intrinsic high cycle fatigue behavior of ultrafine grained pure Cu with stable structure. *Sci China Mater*. **2016**;59:531–537.
- [25] Liu FC, Ma ZY. Influence of tool dimension and welding parameters on microstructure and mechanical properties of friction-stir-welded 6061-T651 aluminum alloy. *Metall Mater Trans A*. **2008**;39:2378–2388.
- [26] McNelley TR, Swaminathan S, Su JQ. Recrystallization mechanisms during friction stir welding/processing of aluminum alloys. *Scr Mater*. **2008**;58:349–354.
- [27] Prangnell PB, Heason CP. Grain structure formation during friction stir welding observed by the ‘stop action technique’. *Acta Mater*. **2005**;53:3179–3192.
- [28] Yazdipour A, Shafiei MA, Dehghani K. Modeling the microstructural evolution and effect of cooling rate on the nanograins formed during the friction stir processing of Al5083. *Mater Sci Eng A*. **2005**;405:277–286.
- [29] Dinaharan I, Kalaiselvan K, Akinlabi ET, et al. Microstructure and wear characterization of rice husk ash reinforced copper matrix composites prepared using friction stir processing. *J Alloys Compd*. **2017**;718:150–160.
- [30] Rezaei MR, Toroghinejad MR, Ashrafizadeh F. Effects of ARB and ageing processes on mechanical properties and microstructure of 6061 aluminum alloy. *J Mater Process Technol*. **2011**;211:1184–1190.
- [31] Kim JK, Jeong HG, Hong SI, et al. Effect of aging treatment on heavily deformed microstructure of a 6061 aluminum alloy after equal channel angular pressing. *Scr Mater*. **2001**;45:901–907.
- [32] Chang SY, Lee KS, Choi SH, et al. Effect of ECAP on microstructure and mechanical properties of a commercial 6061 Al alloy produced by powder metallurgy. *J Alloys Compd*. **2003**;354:216–220.
- [33] Kim WJ, Wang JY. Microstructure of the post-ECAP aging processed 6061 Al alloys. *Mater Sci Eng A*. **2007**;464:23–27.
- [34] Sha G, Tugcu K, Liao XZ, et al. Strength, grain refinement and solute nanostructures of an Al–Mg–Si alloy (AA6060) processed by high-pressure torsion. *Acta Mater*. **2014**;63:169–179.
- [35] Sato YS, Urata M, Kokawa H, et al. Hall–Petch relationship in friction stir welds of equal channel angular-pressed aluminium alloys. *Mater Sci Eng A*. **2003**;354:298–305.
- [36] Myhr O. Modelling of the age hardening behaviour of Al–Mg–Si alloys. *Acta Mater*. **2001**;49:65–75.
- [37] Gómora CM, Ambriz RR, Curiel FF, et al. Heat distribution in welds of a 6061-T6 aluminum alloy obtained by modified indirect electric arc. *J Mater Process Technol*. **2017**;243:433–441.